atmosphere

MDPI

Article

New Setup of the UAS ALADINA for Measuring Boundary Layer Properties, Atmospheric Particles and Solar Radiation

Konrad Bärfuss *, Falk Pätzold, Barbara Altstädter, Endres Kathe, Stefan Nowak, Lutz Bretschneider, Ulf Bestmann and Astrid Lampert

Institute of Flight Guidance, Technische Universität Braunschweig, 38108 Braunschweig, Germany; f.paetzold@tu-braunschweig.de (F.P.); b.altstaedter@tu-braunschweig.de (B.A.); endreskathe@gmail.com (E.K.); stefan.nowak@tu-braunschweig.de (S.N.); l.bretschneider@tu-braunschweig.de (L.B.); u.bestmann@tu-braunschweig.de (U.B.); astrid.lampert@tu-bs.de (A.L.)

* Correspondence: k.baerfuss@tu-braunschweig.de; Tel.: +49-531-391-9805

Received: 29 September 2017; Accepted: 14 January 2018; Published: 17 January 2018

Abstract: The unmanned research aircraft ALADINA (Application of Light-weight Aircraft for Detecting in situ Aerosols) has been established as an important tool for boundary layer research. For simplified integration of additional sensor payload, a flexible and reliable data acquisition system was developed at the Institute of Flight Guidance, Technische Universität (TU) Braunschweig. The instrumentation consists of sensors for temperature, humidity, three-dimensional wind vector, position, black carbon, irradiance and atmospheric particles in the diameter range of ultra-fine particles up to the accumulation mode. The modular concept allows for straightforward integration and exchange of sensors. So far, more than 200 measurement flights have been performed with the robustly-engineered system ALADINA at different locations. The obtained datasets are unique in the field of atmospheric boundary layer research. In this study, a new data processing method for deriving parameters with fast resolution and to provide reliable accuracies is presented. Based on tests in the field and in the laboratory, the limitations and verifiability of integrated sensors are discussed.

Keywords: UAS; RPAS; ALADINA; atmospheric boundary layer; airborne turbulence; radiation measurements; aerosol measurements; field experiments; validation methods

1. Introduction

The use of unmanned aerial systems (UAS), often also called remotely-piloted aircraft systems (RPAS), for atmospheric research has increased significantly over the last few decades. The new setup of ALADINA (Application of Light-weight Aircraft for Detecting in situ Aerosols) in the context of the ongoing development is provided as an introduction to the current modifications. The first applications date back to several decades ago [1]; later, some UAS applications of atmospheric research groups were reported in the 1990s [2]. Compared to these first meteorological applications, there has been a revolution concerning the functionality, size and complexity of even commercially available airborne systems, autopilots and the corresponding hardware and software. Nowadays, UAS are deployed in a broad range of meteorological research fields. The smallest systems with a weight below or slightly exceeding 5 kg are mainly equipped with basic meteorological sensors for measuring humidity and temperature [3]. They can be used comparable to a recoverable radiosonde [4], but have the advantage of performing specific flight patterns, as demonstrated by Hemingway et al. [5], which shows the repeated sampling and analysis of the small-scale atmospheric boundary layer (ABL) phenomena with a multicopter system. Some systems provide measurements of additional parameters, e.g., ozone concentration [6] or the concentration of the greenhouse gases methane and carbon dioxide [7].

There have been significant improvements in the sensors for estimating the basic meteorological parameters. For determining the three-dimensional wind vector in high temporal and high spatial resolution, a miniaturized multi-hole probe (MHP) along with the Global Navigation Satellite System (GNSS) and inertial measurement unit (IMU) has been implemented [8–10]. Using these systems, turbulence parameters can be studied [11] and turbulent fluxes of sensible heat are derived [12]. Other systems use specific flight patterns and assumptions of the influences of wind on UAS to provide an estimate of the wind speed and wind direction in order to derive turbulent fluxes of sensible and latent heat [13,14].

In addition to basic meteorological parameters at high resolution, several systems with a payload weight between 5 and 25 kg rely on miniaturized sensors for measuring aerosol properties. A condensation particle counter in combination with a three-wavelength absorption photometer and chemical sampling has been used by Bates et al. [15]. Another research work includes measurements of longwave and shortwave broadband radiation, total aerosol particle number concentration and size distribution, as well as a video camera [16].

Applications of UAS and meteorological payload are manifold. Various systems have been deployed to study atmospheric particles at different locations. Bates et al. [15] reported measurements at Ny-Ålesund, Svalbard, for studying long-range transport of particles into the Arctic, especially black carbon (BC). The system of de Boer et al. [16] has been developed to study Arctic haze properties in the Alaskan Arctic. Furthermore, applications to perform measurements in thunderstorms and tornadic supercells have been reported [17].

Besides typical short-term missions of meteorologically-equipped systems, other UAS with combustion engines provide the capability of long-range flights, as far as permitted by the authorities. Therefore, they mostly are operated in sparsely-inhabited areas. Such systems have been used for up to 30 h per flight in the Arctic [18], Antarctic [19] and above the Indian Ocean [20]. In addition to the meteorological sensors, remote sensors are employed for monitoring surface properties like ice cover, sea ice type and surface temperature [18].

The next step in the complexity of operations is the simultaneous use of more than one UAS, reported in Ramanathan et al. [20], who coordinated three aircraft measuring total aerosol particle number concentration, soot and radiation related to clouds. UAS operation with two aircraft following different flight patterns was performed as well in the study of Platis et al. [21]. For some meteorological experiments, the advantages of UAS and manned aircraft were combined to complete the overall picture (e.g., Neininger and Hacker [22], Lothon et al. [23]). A recent overview of UAS application for meteorological research and their instrumentation is provided by Elston et al. [24] and Villa et al. [25].

Compared to other platforms, UAS fill a gap between stationary in situ and remote sensing measurement systems like ground-based LiDAR and radar or tethered balloon observations, on the one hand, and on the other hand, manned aircraft, which cover larger distances at higher cruising speed. For repeatedly probing the development of the atmospheric boundary layer on small scales of a few kilometers, UAS are the most cost-efficient and easy to operate devices available. With the ongoing miniaturization of meteorological sensors and electronic components, they achieve the same temporal resolution as in situ observations onboard manned aircraft, and complex light-weight instruments can be included. Additionally, UAS provide the possibility to probe areas too hazardous for manned measurement flights, e.g., in volcanic ash conditions or over sites contaminated by ionizing radiation. Since they fly generally at lower cruising speed (typical 10–30 $m\,s^{-1}$), the spatial resolution is higher compared with manned aircraft (typical cruising speed 50–200 $m\,s^{-1}$) assuming the identical measurement rate.

The UAS ALADINA (Application of Light-weight Aircraft for Detecting in situ Aerosols; the principal shape of the aircraft can be seen in [26]) operated at the Institute of Flight Guidance at TU Braunschweig (Technische Universität Braunschweig) corresponds to the weight class up to 25 kg with a wing span of 3.6 m. The pusher aircraft of type Carolo P360 was designed with the purpose to carry large sensors (sensor volume up to 0.02 m^3) in a specifically-designed payload

bay. To avoid contamination, influence on aerosol measurements and to reduce vibrations, it is electrically powered. The first setup of the UAS ALADINA has already been described in detail [26]. As the measurement system has undergone significant changes and improvements after several extended field experiments [21,26], the current system with additional instrumentation, the new data acquisition system deployed in the project Dynamics-aerosol-chemistry-cloud interaction in West Africa (DACCIWA) [27,28] and careful sensor characterization are presented here.

The overall advantage of the UAS ALADINA is the broad range of sensors installed. Since the research group developing and operating ALADINA has its background in the operation of the Meteorological Mini Aerial Vehicle (M^2AV, [11,12,29,30]) and the operation of the manned research aircraft D-IBUF [31] and its measurement systems and works closely together with the researchers developing and using the Multi-purpose Airborne Sensor Carrier (MASC, [32–34], ALADINA takes advantage of many experiences with those systems and subsystems.

For ALADINA, a preview of the resulting parameters and uncertainties can be found in Table 1, which will be discussed below.

Table 1. Resulting parameters of the UAS(unmanned aerial systems) ALADINA (Application of Light-weight Aircraft for Detecting in situ Aerosols).

Parameter	Symbol	Unit	Uncertainty
position	$\overrightarrow{P}$	m	2.5 m CEP [1]
altitude	$H_{combined}$	m	±0.05 m
static pressure	P_{stat}	Pa	±220 Pa
static temperature	$T_{stat,compl.}$	°C	±0.1 K
static humidity	$m_{RH,compl.}$	% RH	±1.5% RH
dry air density	ρ_{dry}	kg m^{-3}	±0.01 kg m^{-3}
horizontal wind direction	dd	°	±3°
horizontal wind speed	ff	m s^{-1}	±0.2 m s^{-1}
vertical wind speed	w	m s^{-1}	±0.15 m s^{-1}
total aerosol number concentration 7 nm<..< 2 µm	N_7	cm^{-3}	±20% cm^{-3}
total aerosol number concentration 12 nm<..< 2 µm	N_{12}	cm^{-3}	±20% cm^{-3}
size distribution of particles 0.39 µm<..< 10 µm	$N_{390,723,1499,5000}$	cm^{-3}	±15% cm^{-3}
black carbon mass concentration	N_{BC}	µg m^{-3}	±30% µg m^{-3}
shortwave downwelling irradiance	$Q_{\downarrow}$	W m^{-2}	±50 W m^{-2}
shortwave upwelling irradiance	$Q_{\uparrow}$	W m^{-2}	±50 W m^{-2}

[1] Circular error probable.

2. Flight Operation for Atmospheric Research

The operation of the UAS ALADINA in the field requires flat terrain of approximately 50 × 5 m for takeoff and landing (grass, gravel, concrete) and two operators. One acts as a pilot for remotely-piloted takeoff and landing and supervising the flight guided by the autopilot. The second operator supervises the mission at a mobile ground station computer, checking the functionality of the autopilot, the sensors and the plausibility of data using a downlink, which provides preliminary real-time data with a transmission rate of currently 1 Hz to ensure a robust connection. It is limited by transmission bandwidth and signal power considering the power consumption, module weight and local transmission regulations. Access to electricity on site is not mandatory, but recommended in order to recharge the batteries of the aircraft and ground station. The limitation of the overall weight up to 25 kg is intended to minimize the administrative effort for flight permissions, since 25 kg currently states a threshold in operating rules (at least in European countries [7]). The handling of ALADINA is done according to appropriate checklists adopted from professional manned-aircraft operation, to ensure that both the instrumentation and the aircraft functionality are checked and the system is ready for takeoff. After switching on the measurement electronics, the alignment of the magnetic sensor is performed. Through wireless communication, the onboard computer can be connected to the ground station, and the measurements can be remotely started by sending the

appropriate command. Shortly after the manually-piloted takeoff, the autopilot is enabled, flying precisely along the uploaded waypoint list. The autopilot flight control is configured for more precise measurements rather than precise path following. That means constant speed control and altitude control are more important than the horizontal navigation control. Furthermore, there is no additional yaw control to provide continuous air flow on the sensors of the aircraft supported by the directional stability of ALADINA itself. Waypoints can be sent during flight to maintain maximal flexibility and to adopt the flight mission to the scientific task. The typical flight time is around 45 min, limited by the batteries for propulsion (2 × 10 s lithium polymer cells, each 10 Ah, overall capacity 740 Wh) and air temperature. After the manually-piloted landing, the typical turn-around time between two flights (including changing the batteries for propulsion, autopilot and payload, as well as copying the data) needs around 20 min. By recharging batteries in parallel with the flights, more than eight consecutive full duration flights on one day can be performed. In comparison with the original system [26], position lights, which allow the determination of the aircraft attitude to fly safely in weak sunlight conditions or even at night, were newly installed. In addition, removable landing lights can support pilots in estimating height over ground while landing.

3. Validation Methods for UAS Measurements

Since measured and post-processed data have to be validated, it is of importance to discuss and improve validation methods critically due to continuous improvements of sensors and algorithms. Validation methods used by the ALADINA research team and other authors, e.g., [9,21,26,35–37], are summarized in this section regarding their usefulness before being applied on the dataset.

Error propagation calculations:

When calculating error propagation for real systems, the sensor errors and cross-sensitivities have to be known for each flying system. Normally, these values are not constant, but depend on the flight state. The needed sensor values are not given in manuals and datasheets in this detail, as manufacturers often do not know the special conditions of each applicant and provide error values derived from standardized laboratory tests. Error propagation calculation is therefore limited to deepen the knowledge about the system and to obtain total system uncertainty estimates based on sensor errors provided by manufacturers.

Laboratory tests:

Laboratory tests can be used for identifying sensor errors and cross-sensitivities that are not given by the manufacturer. Laboratory calibrations, however, normally do not cover the complete sensor environment during flight. Results are therefore not directly applicable to inflight measurements. As an example, wind tunnel calibrations of pressure probes do not include the flow field around the UAS. Even with the complete UAS installed in a wind tunnel, blockage and wall effects distort the result by a relevant magnitude. Investigating transient maneuvers like turns or the flight in free air turbulence in the laboratory is very expensive.

Numerical simulations:

Simulations can be used to get knowledge of principal sensor behavior, but it is important to include all relevant influences on the sensors in the model. There may remain some unknown influences (cross-correlations and error terms), which can possibly be identified by laboratory tests. Transient simulations of complex systems often require remarkable computational effort.

Comparison of independent sensors:

The comparison of sensors is used to determine the relative differences of the measurements. This comparison must take into account the degree of interdependency between the measurements, considering for instance the measurement task, the sensing principles and the spatial difference. Proclaiming one sensor as the reference requires an assured uncertainty about one magnitude below

the expected uncertainty of the sensor that shall be assessed. Comparisons of inflight measurements with ground-based measurements are affected by the time- and position-dependent environment parameters; e.g., for three-dimensional LiDAR wind measurements, beam velocities of different beam directions are combined to obtain wind vectors and therefore only represent mean velocities over a certain volume (change in time), e.g., Weitkamp [38].

Intrinsic plausibility tests:

Intrinsic plausibility tests rely on the inflight dataset itself examining the theoretically zero correlation between physical independent values, e.g., static air temperature must be uncorrelated to the aircraft attitude, and the vertical wind component in the Earth-fixed reference frame must be uncorrelated to the aircraft phugoid (slow natural oscillation around the transverse aircraft axis resulting in a pitch oscillation) in straight flight. Other common flight maneuvers are repeated wind squares to demonstrate that the horizontal wind determination does not correlate with flight direction and flight speed. Furthermore, ascents, descents and general attitude changes can be used to show uncorrelated measurements. When using such plausibility tests, assumptions have to be made such as nearly constant wind fields or slowly-varying temperatures at identical heights. Furthermore, statistic methods could be used to prove significant independence of, e.g., flight maneuvers on measurements.

Model-based validation (e.g., Kolmogorov's law):

The most favorite model for validating airborne meteorological data is the Kolmogorov law for the power of local isotropic turbulence in the inertial subrange [39]. When using model-based validations, one should make sure that boundary conditions are given. As shown in several papers (e.g., Lampert et al. [11]), the conditions (steady-state, locally isotropic) for the Kolmogorov law may not be given in daytime transition. This causal problem can be moderated by using data obtained in appropriate meteorological conditions. Finally, the compliance of measured turbulent values with the Kolmogorov law is a necessary, but not sufficient criterion.

4. Devices on the UAS ALADINA for Precise Monitoring of Boundary Layer Properties

The new setup of the UAS ALADINA is shown in Figure 1, where sensors and systems are marked and named.

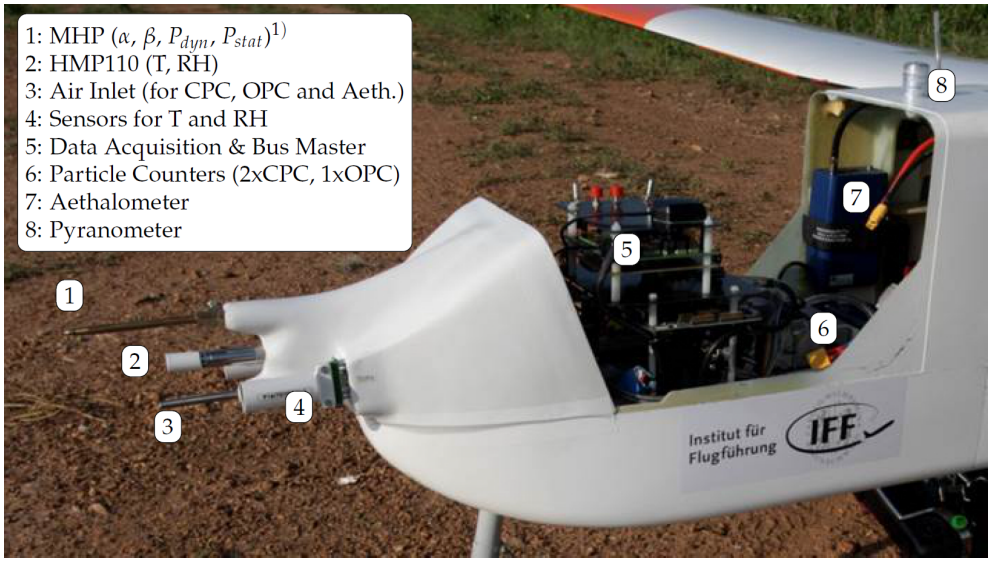

Figure 1. Payload bay of ALADINA with measurement equipment. [1] MHP: multi-hole probe, α: angle of attack, β: angle of sideslip.

A complete meteorological sensor package to determine turbulence data is installed in the nose of ALADINA. This sensor package was re-engineered taking advantage of experiences with the manned aircraft D-IBUF [31], the UAS M^2AV [29], MASC [10] and the sensor package installed in ALADINA before [26]. Compared to the previous setup [26], all sensor interfaces (circuit boards) were redesigned, special housings were added to temperature and humidity sensing elements to make them total air temperature probes known from manned aviation (cf. Section 4.3.1 for more details), MHP tubing was changed, data acquisition changed completely and data processing was redesigned. Only airframe and particle counters remained identical; therefore, no comparison to the setup shown in [26] is done.

In the following, the system to acquire data, the different sensors and the algorithms and procedures used to calculate the final parameters out of the raw data are presented.

To validate measured and derived data, validation methods presented in Section 3 are applied. Temperature and humidity measurements are validated by comparing ascents with descents (intrinsic validation) and by regarding power densities in comparison with theoretical power density slopes (model-based validation). Wind vector plausibility is shown by a wind square, where no correlation between flight direction and wind direction and wind magnitude should be present (intrinsic test), whereas turbulence data plausibility is shown by comparing actual power density slopes with theoretical power density slopes (model-based validation). Total aerosol particle concentration is compared against ground-based measurements (comparison of independent sensors), whereas a profile of black carbon mass concentration measurements is shown (weak intrinsic validation). At the end, pyranometer data are improved by correcting the angle of sun incidence on the sensor caused by attitude (mostly roll) motion (weak intrinsic validation).

4.1. Data Acquisition and Data Bus System

The data acquisition is realized with a bus system consisting of several microcontroller boards with a direct sensor connection and one single-board computer (SBC). A 168-MHz clocked 32-bit microcontroller, based on the ARM Cortex M4 (ARM Limited, Cambridge, UK) architecture is the central part of the boards closely situated to the sensors. The hard real-time programmed microcontrollers capture the digital sensor data at a rate of 100 Hz. An analog sensor signal is acquired by the 24-bit sigma-delta analog-digital converters AD7190 (Analog Devices, Norwood, MA, USA) with a modulator frequency of 64 kHz. By use of its internal analog front-end and noise shaping downsampling filter set to an output data rate of 100 Hz, a noise free resolution of 18 bit can be achieved in the used configuration. The time stamping of the time critical data acquisition is provided by a GNSS-receiver. By signalizing the beginning of a second with a highly precise PPS-signal (pulse-per-second), the bus client microcontrollers are synchronized. The PPS-signal comes directly out of the GNSS-receiver (uBlox, Thalwil, Switzerland) with an accuracy of better than 10 µs. Therefore, the influence of the temperature and the manufacturing of the oscillators on the different boards can be compensated. This allows one to timestamp the data with the precision of a fraction of 1 ms. The sensor data are transferred using a central bus system with a time division multiple access (TDMA) bus arbitration. The use of the EIA-485-A-1998 (Electronic Industries Alliance) standard for serial communication allows data rates of about 3.2 MBits and ensures a fail-safe transmission in an environment where electromagnetic interference cannot be excluded. The SBC reads the data on the bus lines and sequentially writes them on an SD-card. At the end of a flight, the data can be downloaded via an ftp-client over a wireless LAN connection, or the SD-card can be removed and read out on any computer. Online transcoding of the data stream on the SBC allows transmitting relevant data using an XBEE-module to the ground station with a rate of currently 1 Hz.

4.2. Positioning

Inflight position of ALADINA is measured using a miniature MEMS (micro electromechanical system)-based IMU (inertial measurement unit) with INS/GNSS (integrated navigation system/global navigation satellite system) data fusion iμVRU (iMAR, St. Ingbert, Germany). Data are provided via serial transmission.

4.3. Temperature and Humidity

4.3.1. Sensors Installed for Temperature Measurements

Three different sensors are installed in the nose of the aircraft to measure temperature: the widely-used sensor of the type HMP110 (Vaisala, Vantaa, Finland), which is a Pt1000 element, a digital factory-calibrated-sensor of the type TSYS01 (Measurement Specialties, Hampton, VA, USA) and a fine wire sensor fabricated at the Institute of Flight Guidance, TU Braunschweig, completely redesigned based on experiences in [32], are installed. The sensor consists of two measurement channels using 0.0125-mm platinum wires with one wire setup parallel and one wire setup perpendicular to the flow. As a result of the re-engineering of the fine wire sensor, it is well protected by a housing and was used reliably for the whole campaign of DACCIWA (Dynamics-aerosol-chemistry-cloud interaction in West Africa, Knippertz et al. [27]) during more than 30 h of flight time without any break, despite the harsh dusty environment.

To achieve a well-defined sensor environment, housings acting as nozzles have been installed around the temperature and humidity sensing elements. This leads to total pressure conditions granting enough through-flow by an aspect ratio between inflow and outflow area of 1:5. The aspect ratio in combination with the roughness of the sensor circuit board was shown to result in nearly total pressure conditions (more than 90% of total pressure) and flow speeds inside the nozzle of about 20% of the undisturbed flow speed to allow fast measurements by the sensors. This technique is very common for temperature probes mounted on manned aircraft, e.g., the temperature sensor Rosemount Model 101 F. As an example, the nozzle of a temperature sensor can be seen in Figure 2.

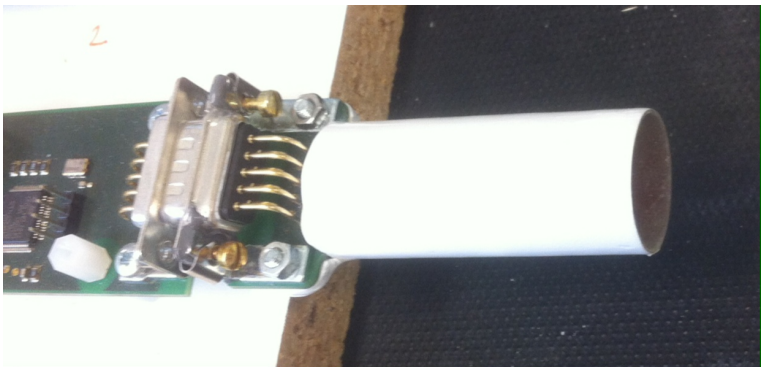

Figure 2. Sensor nozzle for a well-defined environment (total pressure conditions with a well-defined flow rate) for a fine wire temperature sensor. Inside the tube (not visible), the PCB (printed circuit board) to execute raw measurements and carry sensors is installed.

4.3.2. Sensor Fusion of Temperature Measurements

To characterize the ABL, static temperatures are needed, which are temperatures corrected for the warming effect of increased pressure at the sensor's site. Taking into account the dynamic pressure, static values (e.g., static temperature) can be derived accurately from the measured total values. The data of these three sensors can be fused to get both reliable absolute temperature measurements and fast fluctuations.

The relation between total air temperature and static air temperature (both in Kelvin) is given by Equation (1):

$$\frac{T_{total}}{T_{static}} = 1 + \frac{\gamma - 1}{2} Ma^2 \quad (1)$$

where γ (=1.4) denotes the ratio of the heat capacity at constant pressure to the heat capacity at constant volume and Ma denotes the Mach number (both dimensionless quantities).

Complementary filtering is used for fine wire and the factory calibrated readings of the TSYS01 after removing the phase lag. HMP110 sensor readings are only available every second; they were not used for the complementary filtering. Analog output is also available, but the response time is expected to be in the range of the capacitive humidity sensor to allow dew point estimation. Nevertheless, HMP110 temperature measurements can be used as a redundant source. Complementary filtering is done by combining high- and low-pass (Butterworth type, both of first order) filtered measurements. To remove the heat capacity-caused phase lag before on the TSYS01 data, a system with a transfer function of first order is assumed, and readings are filtered with the inverse transfer function. The cutoff frequency of the complementary filters should be lower than the cutoff frequency of the assumed first order system for the reconstruction filter; otherwise, noise may be amplified. The whole process is illustrated by Figure 3.

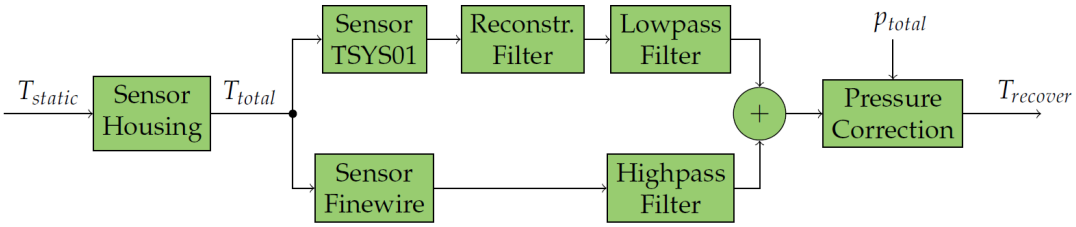

Figure 3. Signal flowchart of the algorithm to recover the total air temperature.

The cutoff frequencies and time constants to filter complementarily and remove phase lag can be derived by taking into account sensor response times (dynamic behavior), which can be determined by comparing ascents and descents or by using more sophisticated techniques, e.g., presented by Tagawa et al. [40].

When two systems with a transfer function of first order and differing time constants can be assumed, every transfer function $T_{meas_i}/T_{air_i} = 1/(1 + \tau_i \cdot s)$, where s denotes the complex frequency domain parameter, only contains one configuration parameter: the time constant τ_i. Since the air temperature is unknown and has to be recovered, these equations cannot be solved directly. The technique presented in [40] solves these two dynamic equations by assuming the same T_{air_i} for both sensors and hence minimizes the mean square difference $\overline{\left(T_{air_1} - T_{air_2}\right)^2}$ of the retrieved air temperature in the frequency domain.

The sensors used showed broad overlap in reliable spectral bands; extracted air temperature therefore consists of the low frequencies measured by the factory-calibrated temperature sensor TSYS01 and the fluctuations recorded by the fast responding fine wire sensor. Errors propagated through the algorithm are attenuated by the applied filters.

4.3.3. Sensors Installed for Humidity Measurements

For humidity measurements, different sensors of the same measuring principle (capacitive) were used, each carefully integrated in a well-defined environment (total pressure conditions with a sufficient flow rate; Figure 2). One is of the type HMP110 (Vaisala, Vantaa, Finland), which is commonly used [41] and often referred to, and a sensing element Rapid P14 (Innovative Sensor Technology, Ebnat-Kappel, Switzerland).

In very humid conditions (RH > 90%), it was shown to be mandatory to seal sensors and electronics close to sensors (e.g., capacitance to digital converters (CDC)) with conformal coating against condensation and water droplets. This allows measuring relative humidity up to 95% at temperatures of about 20 °C without losing accuracy or temporal response. Without sealing, water may influence the overall capacity of the sensor electronics. In more humid conditions, the capacitive measuring principle will not work properly.

4.3.4. Post-Processing of Humidity Measurements

The sensor P14 has been well investigated in Wildmann et al. [42], where a technique has been shown to reconstruct water vapor on the sensor surface by taking advantage of physical modeling. Furthermore, the limitations of this technique have been shown in Wildmann et al. [42]. Because of these limitations, again a first order transfer function for humidity measurements is assumed, and ascents and descents were compared to determine time constants. Since the datasheet describes longer response times for decreasing humidity, one could take into account two time constants: time constant τ_{inc} for increasing humidity and time constant τ_{dec} for decreasing humidity. Complementary filtering (cf. Section 4.3.2) with the long-term stable HMP110 readings and the Rapid P14 data for fluctuations has been performed.

4.3.5. Validation of Temperature and Humidity Results

To check for reliability, Figure 4 shows the power spectra of the sensors used (on the left side temperature, on the right side humidity as the mixing ratio). The power spectra were calculated using the method of Welch [43]. Complementary combined sensor data fit well to the $k^{-5/3}$ power law up to 25 Hz for temperature readings. Since calculation of the mixing ratio depends on temperature, it is shown that relative humidity readings at least do not compromise the spectrum slope. Spectra of relative humidity do not have to follow the $k^{-5/3}$ power law in locally isotropic turbulence in the inertial subrange [39]; therefore, the mixing ratio is used for the spectral roll-off.

To prove reliability, ascents can be compared with descents in the same area, assuming that ABL properties do not change significantly during the time needed for consecutive vertical profiles. Figure 5 (left) shows vertical profiles (ascent with following descent) to prove that no drift and no lag occurs in the retrieved "best guess" temperature after complementary filtering. The phase lag of both HMP110 and TSYS01 can be seen in the top region of the profile around 800 m, where raw measurements describe a smooth curvature around the sharp switch between ascent and descent. Fine wire measurements are not affected by this: indeed, minimal drift can be observed over hours (less than 0.5 K per hour). Therefore, the complementary combined total temperature can be easily converted into a static air temperature with an accuracy of better than 0.1 K. The offset between measurements of the HMP110 and the TSYS01 of 0.2 K has its origin in a pending calibration implementation in the data processing. Figure 5 (right) shows vertical profiles to check data qualitatively against accuracy and phase lag for humidity measurements. Since time constants of the HMP110 and the Rapid P14 sensor only differ minimally and humidity fluctuated fast due to cloud fractions, a phase lag can not be observed in the plot. In both subfigures, it can be seen that raw measurements of slowly-responding sensors depend on the flight pattern, since the ascents and descents were flown by doing turns at constant altitudes followed by straight ascent/descent legs. Complementary filtered values and fast-responding sensors do not inherit these errors.

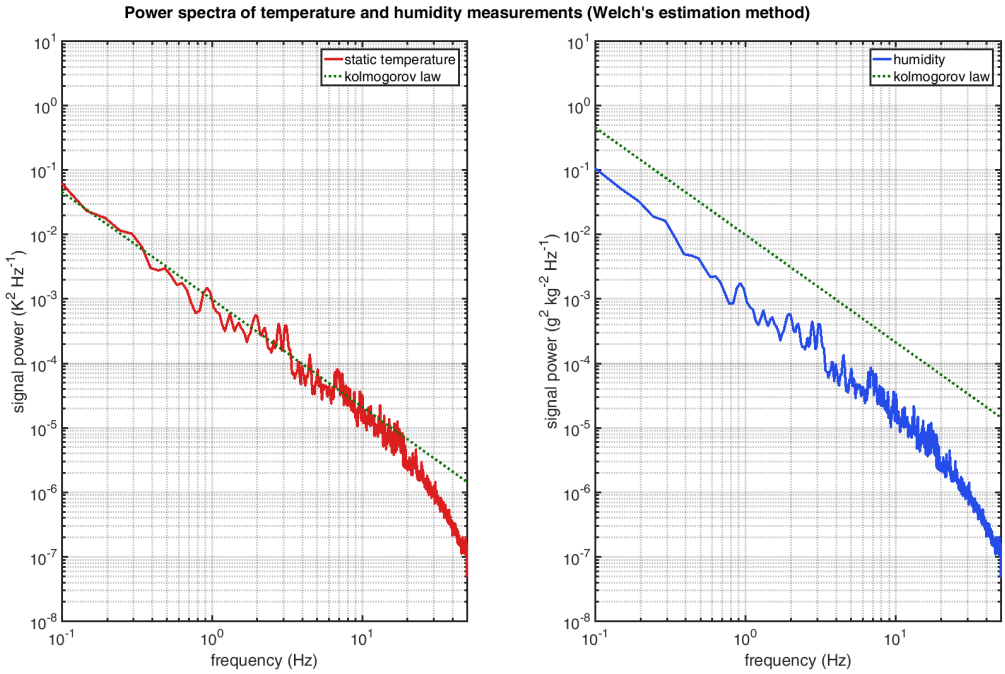

Figure 4. Power spectra of complementary filtered temperature (**left**) and mixing ratio (**right**) using the method of Welch [43] compared to the power law for the inertial subrange of locally isotropic turbulence developed by Kolmogorov [39]. The data were gathered on 2, 10 and 11 July 2016 in Savè (Collines, Benin) during the project Dynamics-aerosol-chemistry-cloud interaction in West Africa (DACCIWA) [27]. Spectra of different straight legs on different days were averaged according to Welch [43].

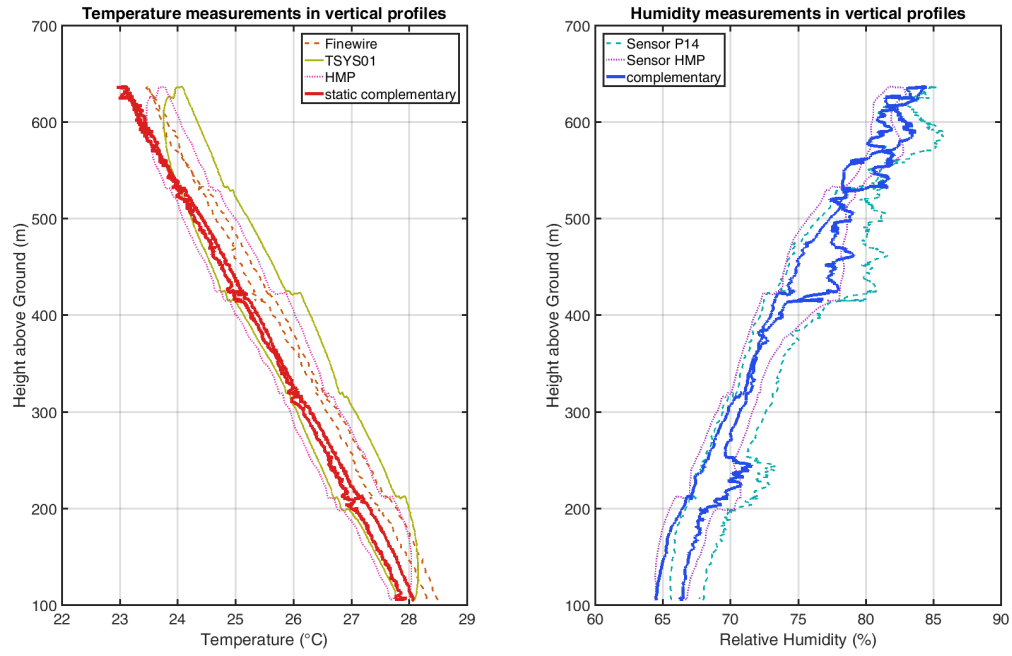

Figure 5. Vertical profiles of temperature (**left**) and humidity (**right**), measured during the project DACCIWA [27] on 15 July 2016 at 06:30 UTC in Savè (Collines, Benin).

4.4. Wind and Turbulence Measurements

4.4.1. MHP to Determine Static Pressure, Dynamic Pressure, Angle of Attack and Angle of Sideslip

A multi-hole probe is installed to determine sideslip angle and angle of attack, airspeed and barometric height. The MHP is calibrated in the wind tunnel with the complete front part of the fuselage of ALADINA (cf. Figure 1), and errors induced by the fuselage are therefore already included in the calibration.

In ALADINA, a miniaturized conical multi-hole probe (MHP) deployed for other different UAS (e.g., Wildmann et al. [10] and Martin et al. [30]) is used to derive dynamic pressure, static pressure, sideslip angle and angle of attack to be able to determine the wind vector. This MHP and its pressure ports are shown in Figure 6. In very humid conditions, small droplets may corrupt measurements of the MHP.

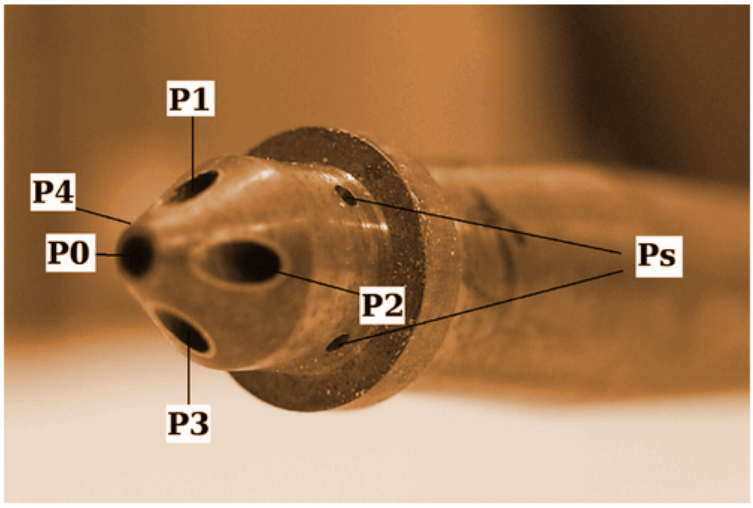

Figure 6. Multi-hole probe with a diameter of 6 mm and its pressure ports designed and manufactured by the Institute of Fluid Dynamics (TU Braunschweig, Germany). Around the central hole *P*0 on the tip, pairs of holes in the vertical (*P*1, *P*3) and horizontal (*P*2, *P*4) axis are visible. In front of the ring, the four small circumferential holes of the static pressure port *Ps* can be seen. Picture taken from [8].

4.4.2. Vector Difference Wind Determination

Raw measurements of the multi-hole probe can be transformed to angle of attack, angle of sideslip, static and dynamic pressure using wind tunnel calibration. Combined with the measured angles of the installed INS/GNSS system, the wind vector with an accuracy of 0.5 m s^{-1} in components at a data rate of 25 Hz is derived according to the formulation shown by Lenschow [44]. The fundamental vector difference equation is:

$$\overline{V}_{w_g} = \overline{V}_{K_g} - \overline{V}_g \tag{2}$$

where $\overline{V}_{w_g}$ denotes the wind vector, $\overline{V}_{K_g}$ the flight path velocity and $\overline{V}_g$ the velocity vector of the aircraft with respect to the air, all three vectors in geodetic coordinates.

Different from the pressure wiring in [8,33], for the new setup of ALADINA, pressure differences from oppositely located holes in the cone of the MHP ($\Delta P_\alpha = P3 - P1$, $\Delta P_\beta = P2 - P4$) are measured directly. The same setup was used by Reineman et al. [45] and other airborne systems [31]. To determine true airspeed, the total pressure at the front hole is measured against the static pressure port ($\Delta P_0 = P0 - Ps$). Short pressure tubes (length < 200 mm) shift resonance effects towards higher, extraneous frequencies ($f_{resonance}$ > 100 Hz). Using this setup, only three difference pressure sensors and one absolute pressure sensor (for the static pressure) are needed.

4.4.3. Enhanced Wind Determination Using Complete Flow Angle Calibration

Small MHP often show discontinuities and non-linear behavior. Normalization to dimensionless pressure coefficients therefore reduces accuracy, since calibration field dependencies on dynamic pressure are neglected. An example of such a calibration field where normalization is not valid is shown in Figure 7. In this figure, vector gradients of the calibration fields for two different calibration TAS (true air speed), 25 m s^{-1} (Figure 7a) and 30 m s^{-1} (Figure 7b), are shown. Since normalization does only affect gradient vectors in value, gradient vector directions have to be identical to allow normalization; this is not the case for the installed probe regarding gradient direction arrows and emphasized isoline curvature in the first quadrant of Figure 7a,b; therefore, normalization would lead to degraded wind vector results.

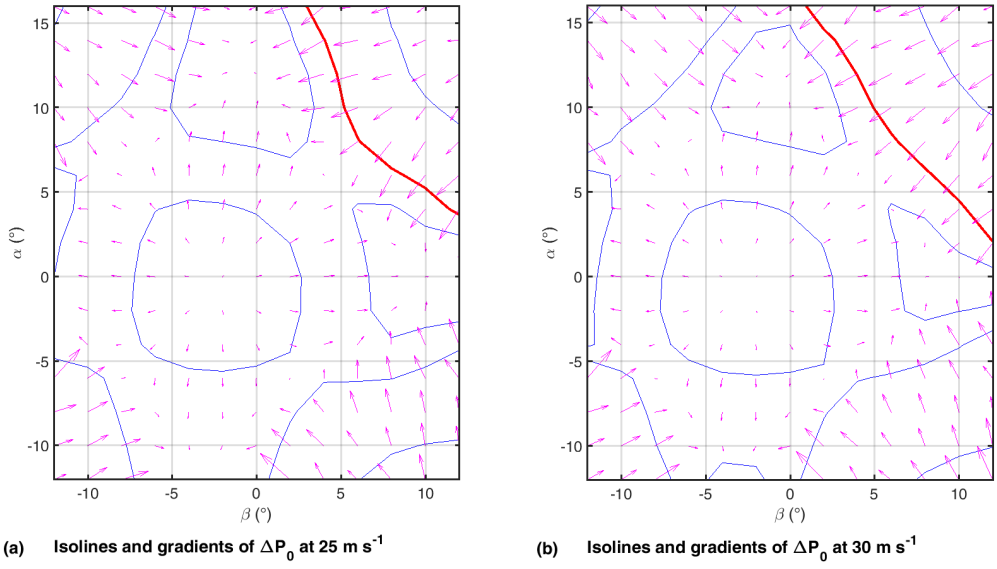

Figure 7. Comparison of calibration field gradients for ΔP_0 at different calibrations P_{dyn} measured in the wind tunnel of Technische Universität (TU) Braunschweig on 20 December 2016. Arrows show the gradients of pressure measurements represented by isolines, depending on sideslip angle β and angle of attack α. (**a**) shows the calibration field for 25 m s^{-1} wind speed, (**b**) for 30 m s^{-1}.

Normalization reduces the three dimensions of a volumetric measurement field, e.g., $\Delta P_\alpha = f\left(\alpha, \beta, P_{dyn}\right)$, into a two-dimensional field $k_\alpha = f\left(\alpha, \beta\right)$ to improve the comprehension of angle measurements. Instead of deriving polynomials only dependent on two (normalized) measurements, one can also derive polynomials in a three-dimensional field. It is not mandatory to use algebraic expression over the whole definition area; a local projection between calibrated values (also known as interpolation) is adequate with respect to other uncertainties in wind vector measurements (e.g., pressure transducers, aircraft attitude). When the measured calibration volume to define the projection between angles and measured pressures (Equation (3)):

$$f : R^3 \rightarrow R^3, \begin{bmatrix} \Delta P_\alpha \\ \Delta P_\beta \\ \Delta P_0 \end{bmatrix} = f\left(\begin{bmatrix} \alpha \\ \beta \\ P_{dyn} \end{bmatrix}\right) \tag{3}$$

is bijective (each element of the left-hand set is paired with exactly one element of the right-hand set and vice versa), which is satisfied by any appropriate design of a calibratable MHP (strong continuous gradients for α, β and P_{dyn}), it is possible to build the inverse function $g = f^{-1}$. This can also be done using algebraic expressions, but much more simply by gridding data in order to generate a directly interpolatable volumetric data field as shown in Equation (4).

$$\begin{bmatrix} \alpha \\ \beta \\ P_{dyn} \end{bmatrix} = g \left(\begin{bmatrix} \Delta P_\alpha \\ \Delta P_\beta \\ \Delta P_0 \end{bmatrix} \right) \tag{4}$$

The resulting subsets $g_i : R^3 \rightarrow R^1$, e.g., $\alpha = g_1 \left(\left[\Delta P_\alpha, \Delta P_\beta, \Delta P_0 \right]^T \right)$ can be interpolated directly. Maximal sensitivity of this interpolation can be obtained by the gradient in each of the three directions. Thus, the maximum gradient is a representative of the maximum amplification of differential pressure measurements. The mentioned subset volume (represented by slices) to determine α is shown in Figure 8 as one given example. It shows the dependency of the resulting angle of attack α on measured pressure differences ΔP_α, ΔP_β and ΔP_0.

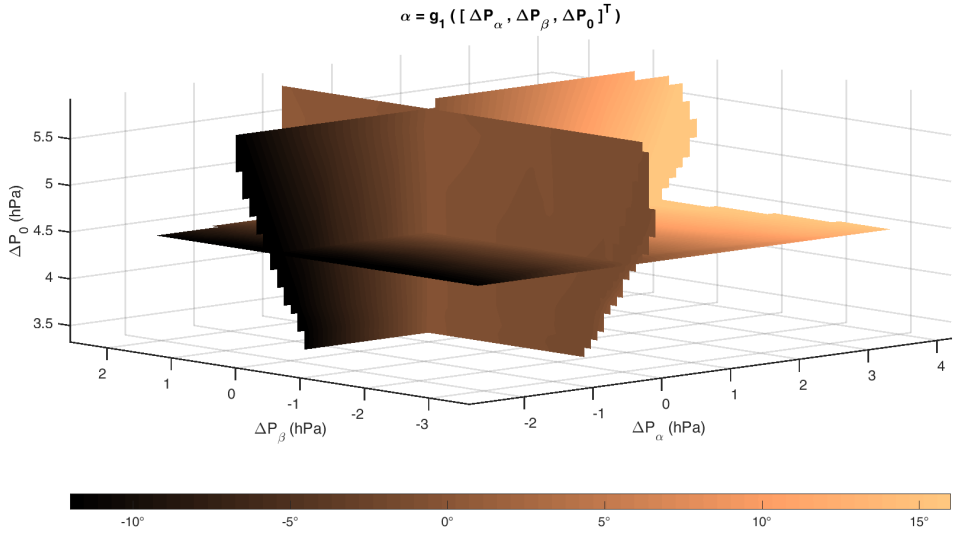

Figure 8. One of the three inverted volumetric calibration data fields (hyper-surfaces) to retrieve dynamic pressure and flow angles out of MHP pressure measurements. Here, slices through the hyper-surface for the angle of attack depending on the three pressure measurements ΔP_α, ΔP_β and ΔP_0 are shown. Dark colors represent negative angles of attack, whereas light colors represent positive angles of attack. Color coding is shown through the color bar below the hyper-surface.

4.4.4. Validation of Wind Vectors Retrieved

The measurement strategy implicated square patterns to validate wind determination. An example of such a pattern and its retrieved wind vectors in the horizontal plane is shown in Figure 9. Measurements during turns are excluded as the rotating flow field around the UAS does influence the calibration significantly compared to straight flight. In addition, the flight state in turn has a significant impact on the pressure field of the MHP; this effect cannot be addressed by a calibration in a wind-tunnel. Further, the retrieval of correct flight attitude out of INS/GNSS data may be subject to large errors during high dynamic maneuvers, as the navigation filter calculating the data fusion is attenuated. In [46], it can be seen that attitude angle deviations between an INS/GNSS system of the same type as used in ALADINA compared to a reference system increase when motion changes from low dynamic to high dynamic. In addition, it is stated in [46] that significantly varying sideslip angles will lead to deviations in roll. This is caused by the algorithm assumption, that there is no lateral velocity with respect to flight track.

Recent data analysis showed that the bottle-neck for wind uncertainty is the accuracy of the IMU [24]. With a more precise and accurate IMU than the current MEMS-IMU (microelectromechanical systems-inertial measurement unit) in addition with more advanced strapdown calculation, wind determination would be improved noticeably.

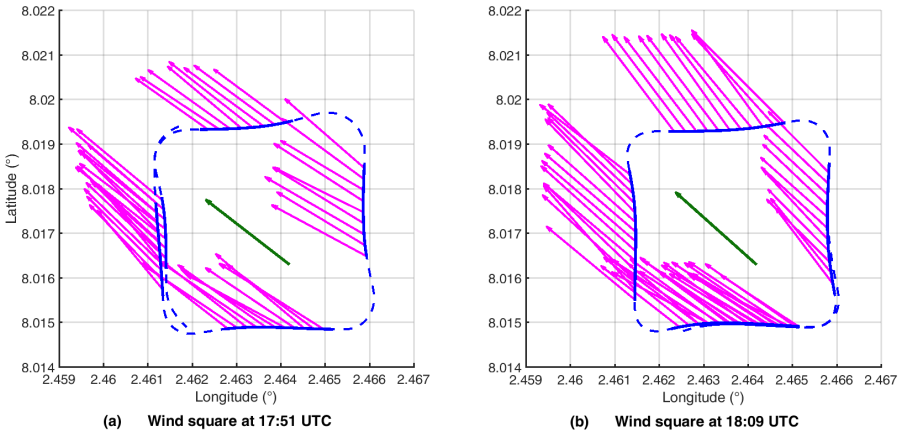

Figure 9. Two examples of wind squares flown and their determined wind vectors (only every 100th vector is shown for readability), measured on 2 July, at 17:51 and 18:09 UTC in Savè (Collines, Benin), during the DACCIWA [27] project at 100 m above the ground. For the wind square in (**a**), mean wind direction was 128° and wind magnitude 2.6 m s^{-1}. For the wind square in (**b**), mean wind direction was 132° and wind magnitude 2.7 m s^{-1}. In each subfigure, the averaged wind vector is shown in dark grey.

4.4.5. Validation of Turbulence Measurements

The ability to measure turbulence data is often shown by a spectral roll-off of calculated wind components. Figure 10 shows the power spectra of the determined wind components. The power spectra were calculated using the method of Welch [43] over three flights with a total data length of 1650 s. Data fit well to the $k^{-5/3}$ power law up to 7 Hz. At higher frequencies, the low-pass filter used for wind calculations attenuates the signal. In the data processing of the pressure sensors used, the authors use at least 10-times oversampling to ensure that amplitude and frequency information is not corrupted by aliasing filter effects.

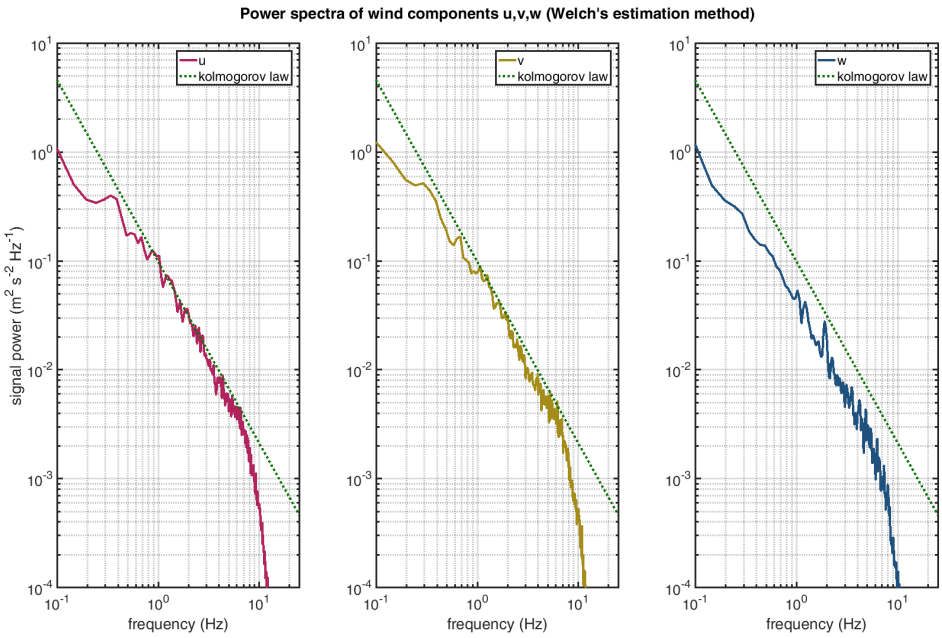

Figure 10. Power spectra of wind components using the method of Welch [43] compared to the power law for the inertial subrange of locally isotropic turbulence developed by Kolmogorov [39]. The data were gathered on 2, 10 and 11 of July 2016 in Savè (Collines, Benin) during the project DACCIWA [27]. Spectra of different straight legs on different days were averaged according to Welch [43].

4.5. Aerosol Characterization and Black Carbon Measurements

4.5.1. Sensors Installed

As presented in Altstädter et al. [26] and Platis et al. [21], ALADINA carries two condensation particles counters (CPCs, Model 3007, TSI Inc., St. Paul, MN, USA) and one optical particle counter (OPC, Model GT-526, Met One Instruments Inc., Washington, DC, USA) in order to classify the total aerosol particle number concentration and size distribution from ultra-fine particles up to particles belonging to the accumulation mode. The inlet is installed at the nose of ALADINA, close to the meteorological instrumentation. Two condensation particle counters of the same type with different threshold diameters are used as indicators for the total aerosol number concentration of freshly-formed particles. The hand-held instruments were miniaturized, tested and calibrated by the project partners of the Leibniz Institute for Tropospheric Research (TROPOS) in Leipzig, Germany. The lowest cut-off sizes were set during the last operation of 7 nm (N_7) and 12 nm (N_{12}), respectively, by a fast resolution of 1.3 s. The OPC operates within six channels from 0.39 µm–10 µm in the particle diameter.

In addition, an aethalometer of the type MicroAeth® Model AE51 (AethLabs, San Francisco, CA, USA) has been installed in ALADINA to measure the BC (black carbon) mass concentration in the range of 0–1 mg m^{-3} with a given resolution of 1 ng m^{-3}. As the instrument is sensitive to vibrations, readings have to be low-pass filtered during post-processing. The accuracy was estimated as ± 0.2 µg m^{-3}.

4.5.2. Validation of Aerosol Concentration and BC Measurements

In order to show the reliability of the system to measure new particle formation, Figure 11 is displayed. The total aerosol particle number concentration in the particle diameter between 7 and 12 µm (N_{7-12}) measured by ALADINA is compared with a ground-based instrument (Twin Scan Mobility Particle Sizer (TSMPS) [47]) that was mounted at the same time during a field study in Melpitz, Germany. During the time period from 10:30–11:55 UTC, four scanning intervals were performed with TSMPS (20 min average) and two measurement episodes with ALADINA from 10:41–11:09 UTC and between 11:12 and 11:30 UTC (1-min interval). During the measurement period, new particle formation occurred and can be seen in the enhanced total aerosol particle number concentration in the small diameter size between 7 and 12 nm. The total maximum of $N_{7-12} = 2.8 \times 10^4$ was taken from the TSMPS at 10:50 UTC. The shapes are consistent; however, the CPCs underestimated the peak given by the difference on average. In total, the uncertainties are within 20%, as stated earlier from laboratory characterization.

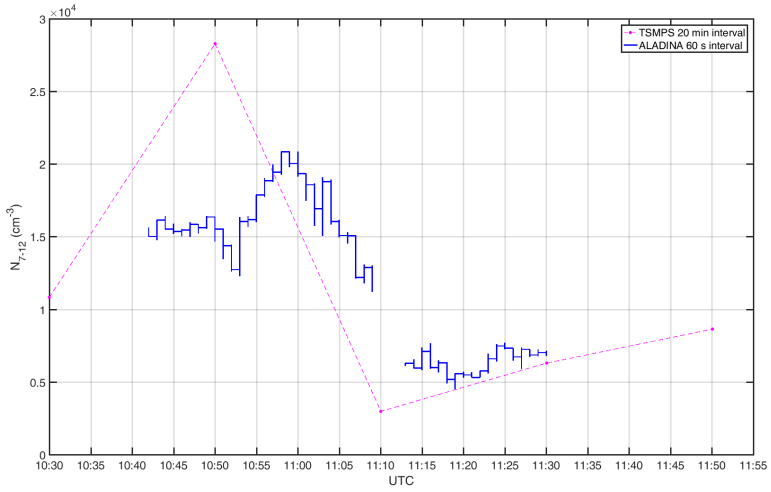

Figure 11. Comparison of the total aerosol particle number concentration in the diameter between 7 and 12 nm measured at the same aerosol inlet with the two condensation particles counters (CPCs) in ALADINA (solid line, 1-min interval) and ground based instrumentation TSMPS (dashed line, 20 min interval) sampling the same air on 21 June 2015 between 10:40 and 11:30 UTC in Melpitz.

Figure 12 shows an example of the significant vertical variability of BC mass concentration, measured during the field campaign in Savè (Collines, Benin) of the DACCIWA project [27]. BC mass concentrations are increasing to a total maximum of 4000 ng m^{-3} between the height of 100 and 300 m. Above and up to the height of 600 m, a significant decline of BC mass concentrations was observed. However, a second enhanced load was measured between the height of 610 and 800 m. The overall investigation was that enhanced BC loads were connected to nocturnal low-level jets and affected by low-level clouds. Further, BC studies influenced by different atmospheric boundary layer properties are still in process. Therefore, the intrinsic validation of BC mass concentration measurements through this likely possible profile is still weak.

During the field experiment in West Africa, harsh environmental conditions (dust, moisture of more than 90% RH, air temperatures higher than 40 °C) showed strong influences on the reliability of the aerosol instrumentation, so that in future perspectives, the sensor package will be insulated in a properly-defined environment.

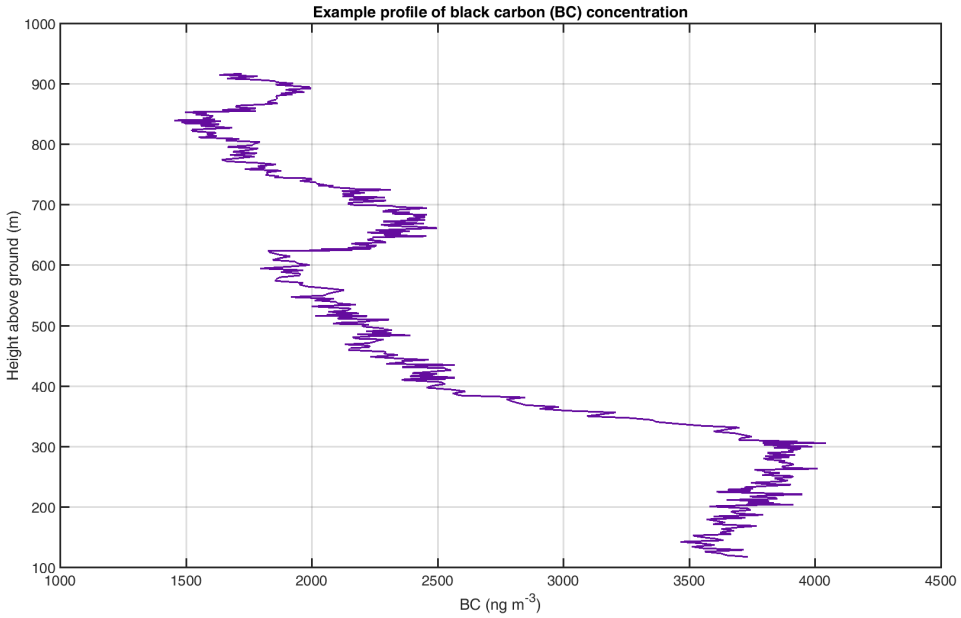

Figure 12. An example of a retrieved vertical profile of BC (black carbon) mass concentration, measured on 15 July, at 06:30 UTC in Savè (Collines, Benin) during the DACCIWA [27] project. An enhanced BC concentration was observed in the lowermost 400 m that was affected by the existence of a nocturnal low-level jet.

4.6. Up- and Down-Welling Irradiance

4.6.1. Pyranometer for Estimating Solar Radiation

In addition to the meteorological and aerosol sensor package, silicium-based pyranometers of the type ML-01 (EKO Instruments, Tokyo, Japan) were installed on the UAS ALADINA: one downward looking and one upward looking with respect to the body-fixed coordinates. The pyranometers show the strong influence of sun incident angle (cf. datasheet) following a cosine law. The pyranometers are mainly used to identify if clouds were present, which is of importance for the interpretation of ABL conditions and aerosol properties. To retrieve shortwave downwelling irradiance, it is possible to calculate the sun incident angle on the sensor and provide a suitable estimation of irradiance values by assuming the cosine law. Since the sun is the only major directional irradiance source in clear sky, restoration of the pyranometer is more complicated on cloudy days. Partly sampled soil and scattering on aerosol particles could also be taken into account, despite their comparably low impact on the sensors.

4.6.2. Basic Correction of Sun Incident Angles on the Pyranometers

Irradiance measurements can be corrected by the angle of incidence γ_{inc} between the pyranometer normal axis and a vector pointing from the Sun to the pyranometers. Using such a correction, attenuated measured irradiance Q_{raw} caused by UAS attitude movements can be recovered to a corrected irradiance Q_{sun} in the direction of the Sun assuming clear skies. The correction applied follows the cosine law for a simple point source of irradiance (Sun on clear skies):

$$Q_{sun} = \frac{Q_{raw}}{\cos(\gamma_{inc})} \tag{5}$$

in addition to a factory calibration curve. The influence of incident angle errors increases with higher incident angles with respect to the sensor axis. The aim of the sun angle of incidence and attitude correction is a transformation of this measurement to an Earth-fixed coordinate system. With another trigonometric transformation using the solar zenith angle Θ_s, the shortwave downwelling irradiance:

$$Q_{\downarrow} = Q_{sun} \cdot \cos(\Theta_s) \tag{6}$$

can now be computed out of Q_{sun}.

4.6.3. Validation of Basic Irradiance Correction

Figure 13 shows the influence of aircraft attitude in pyranometer readings and its correction through the cosine law over the incident angle of the sun with respect to the sensor axis. Figure 13a shows the associated aircraft roll angles, the sun incident angles on the pyranometer sensor axis and the solar zenith angle. The correction of this influence was possible, since this example of measurements took place under almost clear skies. The data were obtained in Savè (Collines, Benin) during the campaign DACCIWA [27] on 11 July 2016. In Figure 13b. one can see a correction of approximately 400 Wm^{-2}. Residual correction errors are mainly caused by degraded attitude measurements during dynamic maneuvers (cf. Section 4.4.4), but the tendency shows that the correlation between irradiance and aircraft attitude (mainly roll angle) can be reduced. Detailed sensor characteristics mentioned in the sensor datasheet were verified by laboratory tests. Secondary sources of errors could be partly sampled soil and scattering on aerosol particles.

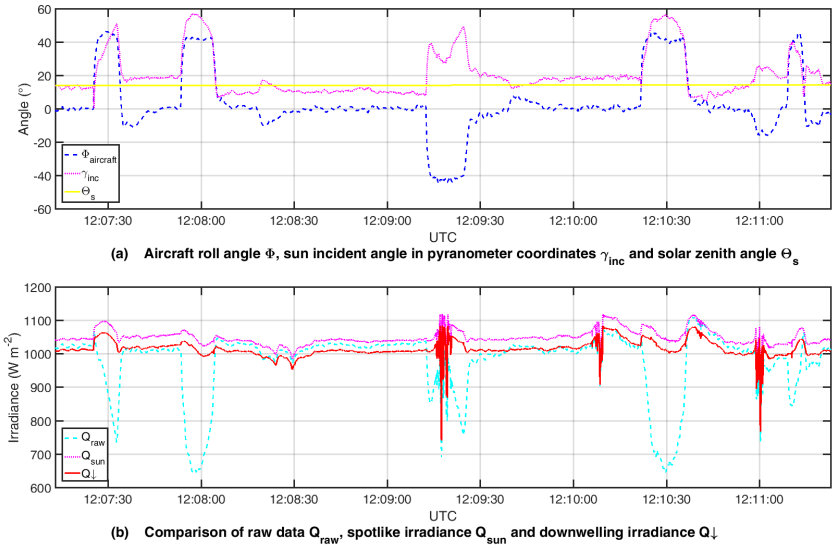

Figure 13. Correction of the sun incident angle on the upward looking pyranometer sensor and shortwave downwelling irradiance, raw data measured on 11 July at 12:10 UTC in Savè (Collines, Benin) during the project DACCIWA [27].

4.7. Overview of the Sensor Package for Measuring ABL Properties

The sensors used on ALADINA are listed in Table 2. Values for response time and accuracy are taken from the manuals of the manufacturers, calibrations and calculations presented in previous articles [8,10,26,32,33].

Table 2. Table of sensors installed in the UAS ALADINA. OPC, optical particle counter.

Parameter	Sensor	Principle	t_{63}	Uncertainty	Source
p, q, r [1)]	iμVRU	IMU	n/a	bias(OTR [2)]) < 0.2° s^{-1}	manual
Φ, Θ, Ψ [3)]	iμVRU	INS/GNSS	n/a	<0.5 deg	manual
$\overrightarrow{v}$ [4)]	iμVRU	INS/GNSS	n/a	n/a	n/a
T_{TSYS}	TSYS01	digital	3 s	±0.1 K	manual
T_{FW}	Fine wire	resistance	<25 ms	1σ < 0.01 K	[32]
T_{HMP}	HMP110	resistance	<5 s	±0.2 K	manual
RH_{HMP}	HMP110	capacity	<7 s	±1.5% RH	manual
RH_{P14}	Rapid P14	capacity	<1.5 s	±1.5% RH	manual
$\Delta P_{0,\alpha,\beta}$ [5)]	AMS 5812-0001-D-B	transd. [6)], MHP	n/a	±15 Pa	manual
Ps	AMS 5812-0150-B	transd. [7)], MHP	n/a	e.g., Table 1	manual
N_7	CPC 1	absorption	n/a	e.g., Table 1	[26]
N_{12}	CPC 2	absorption	n/a	e.g., Table 1	[26]
$N_{390,734,1500,5000}$	OPC	absorption	n/a	e.g., Table 1	[26]
N_{BC}	AE51	absorption	n/a	e.g., Table 1	manual
$Q_{\downarrow}$	Pyr. [8)] EKO ML-01	semicond. [9)] diode	<1 ms	e.g., Table 1	manual
$Q_{\uparrow}$	Pyr.[8)] EKO ML-01	semicond.[9)] diode	<1 ms	e.g., Table 1	manual

[1] angular rates; [2] operating temperature range; [3] attitude; [4] geodetic velocity; [5] used to determine angle of attack α, angle of sideslip β and dynamic pressure; [6] difference pressure transducer; [7] pressure transducer; [8] Pyranometer; [9] semiconductor.

5. Discussion and Future Perspectives

ALADINA with the new data acquisition system proved to be a reliable system during an intense field campaign. The retrieval of data with acceptable errors was demonstrated for a variety of sensors and with different methods. In the near future, the implementation and protection of the vital system components of the particle counters are redesigned to improve handling and calibration during the next campaigns. This resulted in a hermetic and temperature-stabilized enclosure in order to realize reliable operation in extreme conditions, e.g., the Arctic. An active heating system will be added around delicate measurement units. In the near future, wheel brakes in the landing gear to enable operation on even shorter runways will be integrated. To take advantage of a big community, the autopilot system is changed onto a system widely used in the UAS community. Interchangeable telemetry allows ensuring data linkage even at sites with restrictions for high frequencies due to interference with other measurement systems like sensitive telescopes.

Acknowledgments: A special thanks to Birgit Zachrau for valuable support during ALADINA preparation. Thanks to Vanessa Senske for preprocessing campaign data and the support during wind tunnel calibrations. Thanks to Julius Klemm for doing laboratory tests with the pyranometer sensors. Many thanks to Divya Bhatia for proofreading the manuscript.

Author Contributions: K.B., F.P., E.K., U.B. and S.N. developed the new data acquisition and meteorological sensors and integrated the new setup into ALADINA. L.B. was responsible for the flight system, the mechanical sensor integration and the flight operation as the safety pilot. A.L. and B.A. organized the project and were responsible for field campaigns and data analysis. K.B. wrote the paper with the input of all coauthors.

Conflicts of Interest: The authors declare no conflict of interest. The founding sponsors had no role in the design of the study; in the collection, analyses or interpretation of data; in the writing of the manuscript; nor in the decision to publish the results.

References

1. Konrad, T.G.; Hill, M.L.; Rowland, J.R.; Meyer, J.H. A Small, Radio-Controlled Aircraft as a Platform for Meteorological Sensors. *Appl. Phys. Lab. Tech. Digest.* **1970**, *10*, 11–21.
2. Holland, G.J.; Webster, P.J.; Curry, J.A.; Tyrell, G.; Gauntlett, D.; Brett, G.; Becker, J.; Hoag, R.; Vaglienti, W. The Aerosonde Robotic Aircraft: A New Paradigm for Environmental Observations. *Bull. Am. Meteorol. Soc.* **2001**, *82*, 889–901.
3. Reuder, J.; Brisset, P.; Jonassen, M.; Müller, M.; Mayer, S. The small unmanned meteorological observer SUMO: A new tool for atmospheric boundary layer research. *Meteorol. Z.* **2009**, *18*, 141–147.
4. Soddell, J.R.; McGuffie, K.; Holland, G.J. Intercomparison of atmospheric soundings from the aerosonde and radiosonde. *J. Appl. Meteorol.* **2004**, *43*, 1260–1269.
5. Hemingway, B.L.; Frazier, A.E.; Elbing, B.R.; Jacob, J.D. Vertical Sampling Scales for Atmospheric Boundary Layer Measurements from Small Unmanned Aircraft Systems (sUAS). *Atmosphere* **2017**, *8*, 176, doi:10.3390/atmos8090176.
6. Illingworth, S.; Allen, G.; Percival, C.; Hollingsworth, P.; Gallagher, M.; Ricketts, H.; Hayes, H.; Ladosz, P.; Crawley, D.; Roberts, G. Measurement of boundary layer ozone concentrations on-board a Skywalker unmanned aerial vehicle. *Atmos. Sci. Lett.* **2014**, *15*, 252–258.
7. Schuyler, T.J.; Guzman, M.I. Unmanned Aerial Systems for Monitoring Trace Tropospheric Gases. *Atmosphere* **2017**, *8*, 206, doi:10.3390/atmos8100206.
8. Van den Kroonenberg, A.C.; Martin, T.; Buschmann, M.; Bange, J.; Vörsmann, P. Measuring the Wind Vector Using the Autonomous Mini Aerial Vehicle M^2AV. *J. Atmos. Ocean. Technol.* **2008**, *25*, 1969–1982.
9. Thomas, R.M.; Lehmann, K.; Nguyen, H.; Jackson, D.L.; Wolfe, D.; Ramanathan, V. Measurement of turbulent water vapor fluxes using a lightweight unmanned aerial vehicle system. *Atmos. Meas. Tech.* **2012**, *5*, 243–257.
10. Wildmann, N.; Hofsäß, M.; Weimer, F.; Joos, A.; Bange, J. MASC—A small Remotely Piloted Aircraft (RPA) for wind energy research. *Adv. Sci. Res.* **2014**, *11*, 55–61.
11. Lampert, A.; Pätzold, F.; Jiménez, M.A.; Lobitz, L.; Martin, S.; Lohmann, G.; Canut, G.; Legain, D.; Bange, J.; Martínez-Villagrasa, D.; et al. A study of local turbulence and anisotropy during the afternoon and evening transition with an unmanned aerial system and mesoscale simulation. *Atmos. Chem. Phys.* **2016**, *16*, 8009–8021.
12. Martin, S.; Bange, J. The influence of aircraft speed variations on aensible heat-flux measurements by different airborne systems. *Bound. Layer Meteorol.* **2014**, *150*, 153–166.
13. Dias, N.L.; Gonçalves, J.E.; Freire, L.S.; Hasegawa, T.; Malheiros, A.L. Obtaining Potential Virtual Temperature Profiles, Entrainment Fluxes, and Spectra from Mini Unmanned Aerial Vehicles. *Bound. Layer Meteorol.* **2012**, *145*, 93–111.
14. Bonin, T.; Chilson, P.; Zielke, B.; Fedorovich, E. Observations of the early evening boundary-layer transition using a small unmanned aerial system. *Bound. Layer Meteorol.* **2013**, *146*, 119–132.
15. Bates, T.S.; Quinn, P.K.; Johnson, J.E.; Corless, A.; Brechtel, F.J.; Stalin, S.E.; Meinig, C.; Burkhart, J.F. Measurements of atmospheric aerosol vertical distributions above Svalbard, Norway, using unmanned aerial systems (UAS). *Atmos. Meas. Tech.* **2013**, *6*, 2115–2120.
16. De Boer, G.; Palo, S.; Argrow, B.; LoDolce, G.; Mack, J.; Gao, R.-S.; Telg, H.; Trussel, C.; Fromm, J.; Long, C.N.; et al. The Pilatus unmanned aircraft system for lower atmospheric research. *Atmos. Meas. Tech.* **2016**, *9*, 1845–1857.
17. Elston, J.S.; Roadman, J.; Stachura, M.; Argrow, B.; Houston, A.; Frew, E.W. The tempest unmanned aircraft system for in situ observations of tornadic supercells: Design and VORTEX2 flight results. *J. Field Robot.* **2011**, *28*, 461–483.
18. Curry, J.A.; Maslanik, J.; Holland, G.; Pinto, J. Applications of Aerosondes in the Arctic. *Bull. Am. Meteorol. Soc.* **2004**, *85*, 1855–1861.
19. Cassano, J.J.; Seefeldt, M.W.; Palo, S.; Knuth, S.L.; Bradley, A.C.; Herrman, P.D.; Kernebone, P.A.; Logan, N.J. Observations of the atmosphere and surface state over Terra Nova Bay, Antarctica, using unmanned aerial systems. *Earth Syst. Sci. Data* **2016**, *8*, 115–126.
20. Ramanathan, V.; Ramana, M.V.; Roberts, G.; Kim, D.; Corrigan, C.; Chung, C.; Winker, D. Warming trends in Asia amplified by brown cloud solar absorption. *Nature* **2007**, *448*, 575–578.

21. Platis, A.; Altstädter, B.; Wehner, B.; Wildmann, N.; Lampert, A.; Hermann, M.; Birmili, W.; Bange, J. An observational case study on the influence of atmospheric boundary layer dynamics on the new particle formation. *Bound. Layer Meteorol.* **2016**, *158*, 67–92.
22. Neininger, B.; Hacker, J.M. Manned or unmanned—Does this really matter? In Proceedings of the International Conference on Unmanned Aerial Vehicles in Geomatics (UAV-g), Zurich, Switzerland, 14–16 September 2011; Volume XXXVIII-1/C22.
23. Lothon, M.; Lohou, F.; Pino, D.; Couvreux, F.; Pardyja, E.R.; Reuder, J.; Vilà-Guerau de Arellano, J.; Durand, P.; Hartogensis, O.; Legain, D.; et al. The BLLAST field experiment: Boundary-Layer Late Afternoon and Sunset Turbulence. *Atmos. Chem. Phys.* **2014**, *14*, 10931–10960.
24. Elston, J.; Argrow, B.; Stachura, M.; Weibel, D.; Lawrence, D.; Pope, D. Overview of Small Fixed-Wing Unmanned Aircraft for Meteorological Sampling. *J. Atmos. Ocean. Technol.* **2015**, *32*, 97–115.
25. Villa, T.F.; Gonzalez, F.; Miljievic, B.; Ristovski, Z.D.; Morawska, L. An overview of small unmanned aerial vehicles for air quality measurements: Present applications and future prospectives. *Sensors* **2016**, *16*, 1072, doi:10.3390/s16071072.
26. Altstädter, B.; Platis, A.; Wehner, B.; Scholtz, A.; Wildmann, N.; Hermann, M.; Käthner, R.; Baars, H.; Bange, J.; Lampert, A. ALADINA—An unmanned research aircraft for observing vertical and horizontal distributions of ultrafine particles within the atmospheric boundary layer. *Atmos. Meas. Tech.* **2015**, *8*, 1627–1639.
27. Knippertz, P.; Coe, H.; Chiu, J.C.; Evans, M.J.; Fink, A.H.; Kalthoff, N.; Liousse, C.; Mari, C.; Allan, R.P.; Brooks, B.; et al. The DACCIWA project: Dynamics-aerosol-chemistry-cloud interactions in West Africa. *Bull. Am. Meteorol. Soc.* **2015**, *96*, 1451–1460.
28. Bärfuss, K.; Pätzold, F.; Hecker, P.; Lampert, A. DACCIWA Savè super site. Atmospheric boundary layer properties and BC measured with the unmanned research aircraft ALADINA of the TU Braunschweig. *SEDOO OMP* **2017**, doi:10.6096/baobab-dacciwa.1701.
29. Martin, S.; Bange, J.; Beyrich, F. Meteorological profiling of the lower troposphere using the research UAV "M^2AV Carolo". *Atmos. Meas. Tech.* **2011**, *4*, 705–716.
30. Martin, S.; Beyrich, F.; Bange, J. Observing Entrainment Processes Using a Small Unmanned Aerial Vehicle: A Feasibility Study. *Bound. Layer Meteorol.* **2014**, *150*, 449–467.
31. Corsmeier, U.; Hankers, R.; Wieser, A. Airborne turbulence measurements in the lower troposphere onboard the research aircraft Dornier 128-6, D-IBUF. *Meteorol. Z.* **2001**, *10*, 315–329.
32. Wildmann, N.; Mauz, M.; Bange, J. Two fast temperature sensors for probing of the atmospheric boundary layer using small remotely piloted aircraft (RPA). *Atmos. Meas. Tech.* **2013**, *6*, 2101–2113.
33. Wildmann, N.; Ravi, S.; Bange, J. Towards higher accuracy and better frequency response with standard multi-hole probes in turbulence measurement with remotely piloted aircraft (RPA). *Atmos. Meas. Tech.* **2014**, *7*, 1027–1041.
34. Wildmann, N.; Rau, G.A.; Bange, J. Observations of the Early Morning Boundary-Layer Transition with Small Remotely-Piloted Aircraft. *Bound. Layer Meteorol.* **2015**, *157*, 345–373.
35. Baserud, L.; Reuder, J.; Jonassen, M.O.; Kral, S.T.; Paskyabi, M.B.; Lothon, M. Proof of concept for turbulence measurements with the RPAS SUMO during the BLLAST campaign. *Atmos. Meas. Tech.* **2016**, *9*, 4901–4913.
36. Calmer, R.; Roberts, G.; Preissler, J.; Derrien, S.; O'Dowd, C. 3D Wind Vector Measurements using a 5-hole Probe with Remotely Piloted Aircraft. *Atmos. Meas. Tech. Discuss.* **2017**, under review, doi:10.5194/amt-2017-233.
37. Witte, B.M.; Singler, R.F.; Bailey, S.C. Development of an Unmanned Aerial Vehicle for the Measurement of Turbulence in the Atmospheric Boundary Layer. *Atmosphere* **2017**, *8*, 195, doi:10.3390/atmos8100195.
38. Weitkamp, C. *Lidar: Range-Resolved Optical Remote Sensing of the Atmosphere*; Springer Science & Business: Berlin, Germany, 2005; Volume 102.
39. Kolmogorov, A.N. The local structure of turbulence in incompressible viscous fluid for very large Reynolds numbers. *Dokl. Akad. Nauk SSSR* **1941**, *30*, 299–303.
40. Tagawa, M.; Kato, K.; Ohta, Y. Response compensation of temperature sensors: Frequency-domain estimation of thermal time constants. *Rev. Sci. Instrum.* **2003**, *74*, 3171–3174.
41. Ingleby, B.; Moore, D.; Sloan, C.; Dunn, R. Evolution and Accuracy of Surface Humidity Reports. *J. Atmos. Ocean. Technol.* **2013**, *30*, 2025–2043.

42. Wildmann, N.; Kaufmann, F.; Bange, J. An inverse-modelling approach for frequency response correction of capacitive humidity sensors in ABL research with small remotely piloted aircraft (RPA). *Atmos. Meas. Tech.* **2014**, *7*, 3059–3069.
43. Welch, P.D. The use of Fast Fourier Transform for the estimation of power spectra: A method based on time averaging over short, modified periodograms. *Trans. Audio Electroacoust.* **1967**, *15*, 70–73.
44. Lenschow, D.H. *The Measurement of Air Velocity and Temperature Using the NCAR Buffalo Aircraft Measuring System*; NCAR-TN/EDD-74; National Center for Atmospheric Research: Boulder, CO, USA, 1972; Volume 39.
45. Reineman, B.D.; Lenain, L.; Statom, N.M.; Melville, W.K. Development and Testing of Instrumentation for UAV-Based Flux Measurements within Terrestrial and Marine Atmospheric Boundary Layers. *J. Atmos. Ocean. Technol.* **2013**, *30*, 1295–1319.
46. Hinüber, E.V.; Knedlik, S.; Bestmann, U. Low Weight COTS based Inertial Navigation Systems with EASA Certification Potential for UAVs, General Aviation and Military Aircraft. In Proceedings of the 6th UAV World Conference at AIRTEC, Frankfurt/Main, Germany, 6–8 November 2012.
47. Wiedensohler, A.; Birmili, W.; Nowak, A.; Sonntag, A.; Weinhold, K.; Merkel, M.; Wehner, B.; Tuch, T.; Pfeifer, S.; Fiebig, M.; et al. Mobility particle size spectrometers: Harmonization of technical standards and data structure to facilitate high quality long-term observations of atmospheric particle number size distributions. *Atmos. Meas. Tech.* **2012**, *5*, 657–685.